Digest Journal of Nanomaterials and Biostructures

Dig. J. Nanomater. Bios. **2026**; 21(4): 56453
https://doi.org/10.31083/DJNB56453

Original Research

Amorphous Tungsten Sulfide Quantum Dots: Ultrasonic Exfoliation and Photoluminescence Properties

Leilei Lan[1,2,*], Yutong Men[1], Juan Gao[1], Baichun Yao[2], Xingce Fan[3], Guoqun Li[3,*]

[1]School of Mechanics and Optoelectronic Physics, Anhui University of Science and Technology, 232001 Huainan, Anhui, China
[2]Technical Department, Tianneng Battery (Wuhu) Co., Ltd., 241000 Wuhu, Anhui, China
[3]Key Laboratory of Quantum Materials and Devices of Ministry of Education, School of Physics, Southeast University, 211189 Nanjing, Jiangsu, China
*Correspondence: leileilan@aust.edu.cn (Leilei Lan); liguoqun0509@163.com (Guoqun Li)

Academic Editor: Aniello Pelella
Submitted: 28 July 2026 Revised: 14 October 2026 Accepted: 19 October 2026 Published: 11 November 2026

Abstract

Background: Transition metal dichalcogenides (TMDCs) exhibit advantageous optical, electrical, and mechanical properties. In particular, amorphous TMDC quantum dots (QDs) show unique behavior due to their amorphous structure and quantum confinement effect. **Methods:** Amorphous tungsten sulfide (WS_2) QDs were synthesized using liquid-phase ultrasonic exfoliation. **Results:** The QDs (average diameter = 2.2 nm, thickness = 1–3 nm) exhibited an amorphous nature, an optical band gap (3.01 eV) exceeding that of bulk WS_2 (mainly owing to quantum confinement effect), and excitation wavelength–dependent photoluminescence tentatively attributed to the recombination of carriers from localized states. **Conclusions:** This work provides a simple route to size-uniform amorphous WS_2 QDs holding promise for optoelectronic applications.

Keywords: amorphous; tungsten sulfide; quantum dots; photoluminescence

1. Introduction

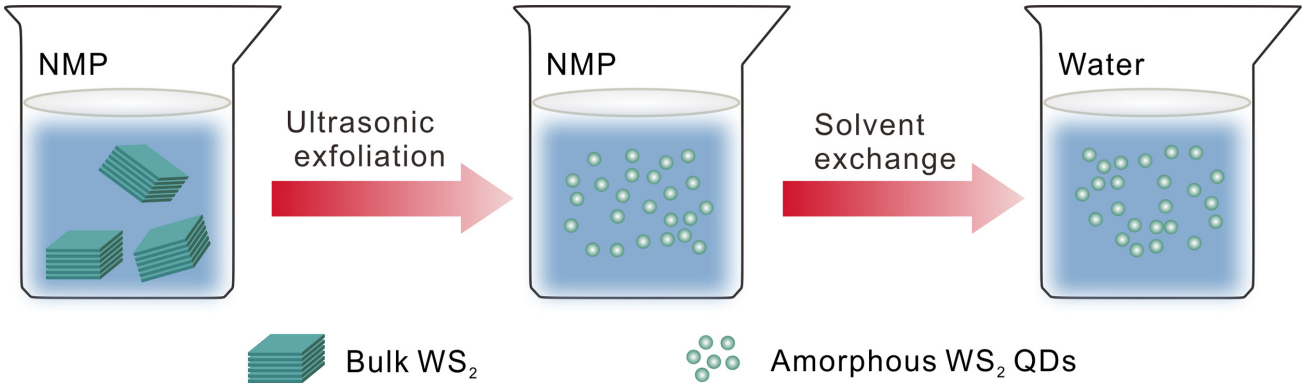
As an emerging class of low-dimensional materials, transition metal dichalcogenides (TMDCs) have gained significant attention for fundamental studies and great potential applications in electronics, optoelectronics, energy storage, catalysis, and biosensing owing to their intrinsic properties [1,2,3,4,5]. TMDCs are compounds of the general formula MX_2, where M is a transition metal element of groups IV-VII B (Mo, W, V, Nb, and so on) and X represents the chalcogen element (S, Se or Te) [6]. The X-M-X unit layer is composed of one layer of transition metal M sandwiched by two atomic layers of chalcogens X. As a layered crystal structure with strong in-plane bonding and weak interlayer van der Waals forces, TMDCs could be easily exfoliated into few layers or monolayers from their bulk materials, resulting in unique properties [7,8,9].

When the size of a material is sufficiently small, its energy levels can be modulated by the quantum confinement effect. This effect can occur once the material size is less than the exciton Bohr radius. Such quantum-confined nanomaterials can be categorized into zero-dimensional (0D), one-dimensional (1D), and two-dimensional (2D) materials [10]. These quantum-confined materials exhibit promising applications in various fields. For example, Soltabayev et al. [11] reported that 2D ZnO nanosheets exhibited excellent CO_2 gas sensing performance. As a class of nanomaterials with sizes usually smaller than 10 nm, quantum dots (QDs) are remarkable because their minute size creates a physically confined electron cloud [12]. The as-prepared QDs are usually regarded as 0D materials. Compared with 1D, 2D and bulk materials, QDs have unique optical, electronic and chemical properties, such as better dispersibility in aqueous media, novel luminescence, easier functionalization, and a higher surface-to-volume ratio [13,14]. Based on these properties, TMDC QDs have become promising nanoparticles for applications in photodetectors [15], medical diagnosis [16], chemical sensors [17], solar cells [18] and so on [4]. For example, Kundu et al. [15] developed a hybrid 2D/QD MoS_2-PbSe broadband photodetector with high sensitivity and room-temperature operation at 2.5 μm. Lian et al. [18] demonstrated that a $MoSe_2$ QD-modified hole extraction layer enables binary organic solar cells with improved efficiency and stability.

Tungsten sulfide (WS_2) QDs, one type of TMDC QDs, have attracted tremendous interest owing to their size-tunable band gaps and remarkable optoelectronic properties. For instance, functionalized fluorescent WS_2 QDs could be used as an optical sensor with high sensitivity and selectivity for ferric ions [19]. A broad-spectrum photodetector was fabricated by using hybrid 0D-3D WS_2-graphene heterojunctions [20]. So far, WS_2 QDs have been synthesized by a number of methods, such as liquid-phase sonication [21], hydrothermal synthesis [22,23], and pulsed laser ablation [24,25]. For example, Cheng et al. [23] reported a hydrothermal-assisted grinding approach to prepare WS_2 QDs from nanosheets. Lee et al. [26] reported the fabrication of WS_2 QDs via a colloidal synthesis method at 300 ℃. However, most of these reported WS_2 QDs exhibit crystalline structures, whereas the preparation of amorphous WS_2 QDs is rarely investigated. The long-range disordered

Copyright: © 2026 The Author(s). Published by IMR Press.
This is an open access article under the CC BY 4.0 license.

Publisher's Note: IMR Press stays neutral with regard to jurisdictional claims in published maps and institutional affiliations.



Scheme 1. Schematics of the preparation process of amorphous WS_2 QDs. QDs, quantum dots; NMP, N-methyl-2-pyrrolidone.

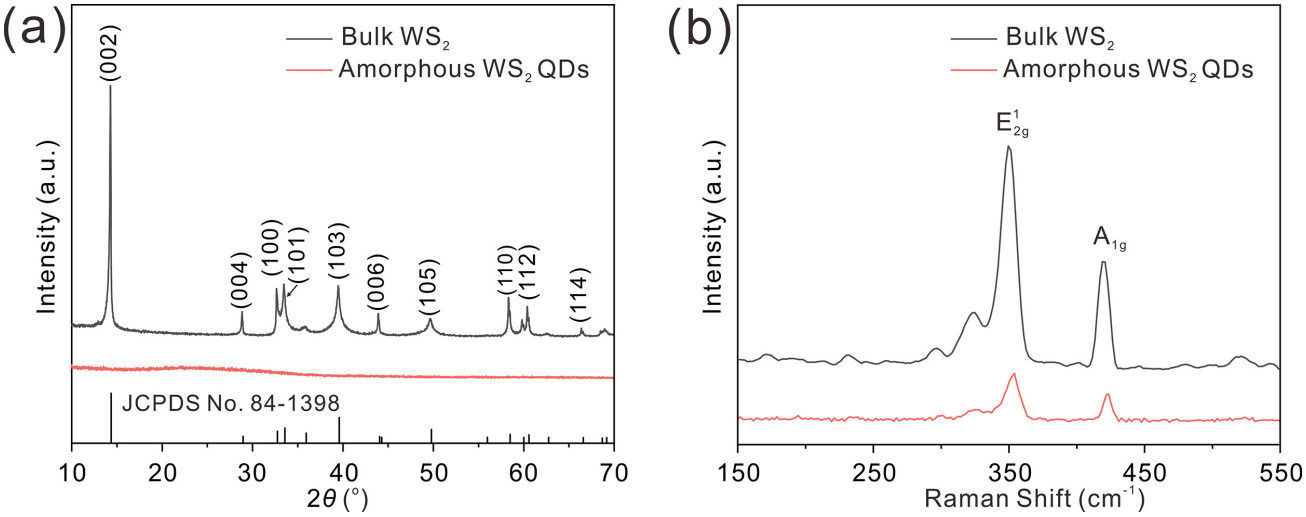


Fig. 1. XRD patterns and Raman spectra of bulk WS_2 and amorphous WS_2 QDs. (a) XRD patterns, (b) Raman spectra. XRD, X-ray diffraction.

structure of amorphous materials can create band tails and dangling bonds, which could produce numerous metastable electronic states [27]. The combination of an amorphous structure with the quantum confinement effect in WS_2 QDs may create specific physical and chemical properties.

Herein, we report a facile exfoliation process for amorphous WS_2 QDs from bulk material through an ultrasonic liquid-phase exfoliation method. A series of techniques such as X-ray diffraction (XRD), X-ray photoelectron spectroscopy (XPS), transmission electron microscopy (TEM), and Raman spectroscopy were used to characterize the as-prepared WS_2 QDs. XRD and selected area electron diffraction (SAED) patterns suggest that the obtained WS_2 QDs exhibit an amorphous nature after exfoliation. The as-prepared WS_2 QDs exhibit a narrow size distribution, with an average diameter of 2.2 nm and a thickness ranging from 1 to 3 nm. Excitation wavelength-dependent photoluminescence (PL) could be observed in these amorphous WS_2 QDs. Our work provides guidance for amorphous WS_2 QD studies to meet the increasing demands in optoelectronic applications.

2. Materials and Methods

2.1 Preparation of Amorphous WS_2 QDs

N-methyl-2-pyrrolidone (NMP, 99.5%, GR) and bulk WS_2 (99.9%, metal basis, 2 μm size) were purchased from Aladdin Co., Ltd. (Shanghai, China). The WS_2 powders were dispersed in 5 mL NMP with an initial concentration of 50 mg/mL. After grinding for 30 min, the dispersion was transferred to a glass vial containing 20 mL NMP. The dispersion was then treated with a sonic tip (XO-SM50, Nanjing, China, 25 kHz, 50% duty cycle, operating mode with 1 s ultrasound followed by 1 s rest interval) with a 6 mm-diameter probe at 300 W for 30 min in an ice bath, followed by bath sonication (KQ3200, Kunshan, China, 40 kHz, 100 W) for another 3 h under ice-bath conditions. The temperature was maintained at 0–10 °C during sonication. The resultant dispersion was centrifuged at 8000 rpm (corresponding to 7104 ×g) for 15 min. Subsequently, the supernatant was carefully collected and filtered using a PTFE filter with a pore size of 0.22 μm. Finally, WS_2 QDs were obtained via dialysis using a membrane with a molecular weight cutoff of 1000 Da for 2 days, during which the deionized water

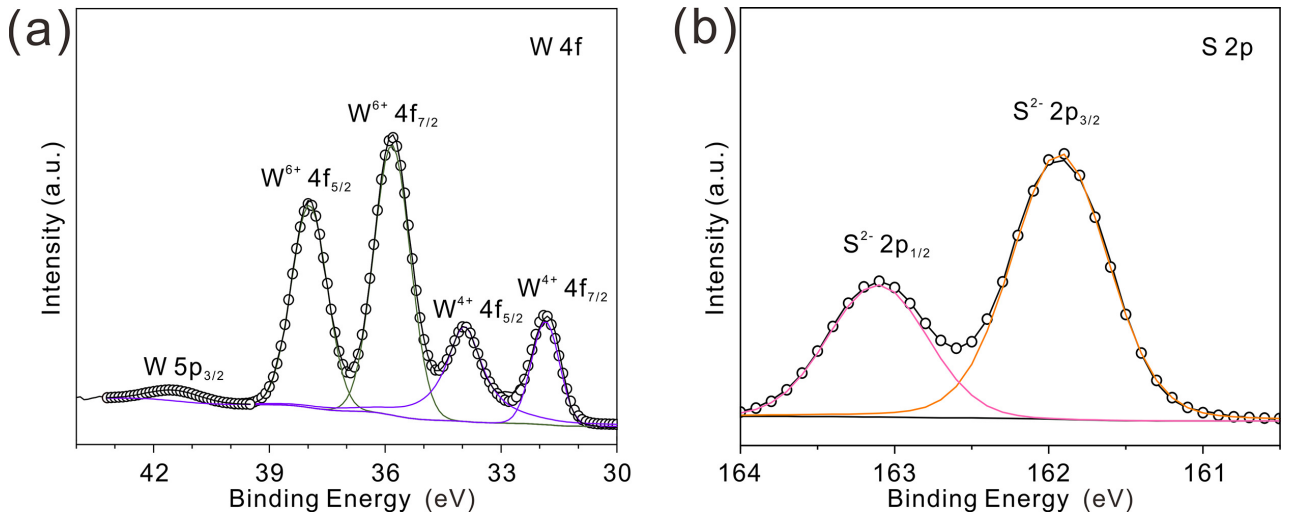


Fig. 2. XPS spectra of amorphous WS_2 QDs. (a) W 4f XPS spectrum, (b) S 2p XPS spectrum. XPS, X-ray photoelectron spectroscopy.

was refreshed every 8 h (Scheme 1). The yield of the WS_2 QDs was about 2.0%. After the WS_2 QDs were dispersed in water, the resulting concentration was 0.5 mg/mL. A total of five independent synthesis batches were performed.

2.2 Characterization

XRD data were acquired using a Rigaku SmartLab (3) X-ray diffractometer (Tokyo, Japan) equipped with Cu Kα radiation (λ = 0.1542 nm) in the 2θ range of 10–70°. TEM images were collected on an FEI Talos F200X TEM (Hillsboro, OR, USA) operated at 200 kV. Atomic force microscopy (AFM) images were obtained using a Bruker Dimension Icon (Billerica, MA, USA). XPS measurements were performed with a Thermo Fisher ESCALAB 250Xi apparatus (Waltham, MA, USA), where the binding energy was calibrated against the C 1s peak at 284.8 eV. The optical absorption properties were measured using a Shimadzu UV-3600 spectrophotometer (Kyoto, Japan). A standard quartz cuvette with an optical path length of 1 cm was used for the UV-Vis absorption measurements. PL properties were investigated using a Horiba Jobin Yvon Fluorolog-3 spectrometer (Irvine, CA, USA) equipped with a Xe lamp at room temperature. PL spectra were corrected for excitation power and detector response.

3. Results

XRD patterns of bulk WS_2 and WS_2 QDs are shown in Fig. 1a. Before ultrasonic exfoliation, several diffraction peaks at 14.3, 28.8, 32.7, 33.5, 39.5, 43.9, 49.7, 58.3, 60.4, and 66.4° are observed in the XRD pattern of bulk WS_2, which can be indexed to (002), (004), (100), (101), (103), (006), (105), (110), (112), and (114) crystal planes of the WS_2 crystal (JCPDS No. 84-1398, $P6_3/mmc$ space group), respectively [28]. After exfoliation and ultrasonication, no peaks are observed in the XRD pattern of WS_2 QDs, suggesting the ultra-small and amorphous structure of the WS_2 QDs. Further structural characterization was performed via Raman spectroscopy in the range from 150 to 550 cm^{-1}. As shown in Fig. 1b, the characteristic Raman peaks at ~350 and ~420 cm^{-1} are attributed to in-plane (E^1_{2g}) and out-of-plane (A_{1g}) active modes of WS_2, respectively [29]. In addition, the Raman intensity of WS_2 QDs is much weaker, further indicating the amorphous nature of WS_2 QDs, which is consistent with XRD data.

XPS measurements were carried out to investigate the chemical composition and band states of the as-synthesized WS_2 QDs. The XPS survey spectrum of amorphous WS_2 QDs clearly displays the characteristic photoemission peaks assigned to W, S, O, and C elements (**Supplementary Fig. 1**). As shown in Fig. 2a, the high-resolution W 4f XPS spectrum of WS_2 can be fitted with two spin-orbit doublets, corresponding to the W^{6+} and W^{4+}. The peaks at 31.85 and 33.95 eV can be assigned to W^{4+} $4f_{7/2}$ and W^{4+} $4f_{5/2}$. The peaks located at 35.82 and 37.96 eV belong to W^{6+} $4f_{7/2}$ and W^{6+} $4f_{5/2}$, respectively [30]. In addition, the peak at 41.50 eV can be assigned to W $5p_{3/2}$ [31]. For the S 2p XPS spectrum (Fig. 2b), the peaks at 161.91 and 163.11 eV originate from the S^{2-} $2p_{3/2}$ and S^{2-} $2p_{1/2}$, respectively. The O 1s spectrum of the amorphous WS_2 QDs shows peaks at 530.33, 531.62, 532.51, and 533.49 eV (**Supplementary Fig. 2**), which are assigned to WO_3, WO_xS_y, SO_4^{2-}, and adsorbed species, respectively [32,33]. The W/S atomic ratio and the relative percentages of W^{4+} and W^{6+} are calculated from the peak areas of each component. For amorphous WS_2 QDs, the relative proportions of W^{4+} and W^{6+} are 31.7% and 68.3%, respectively, with a W/S atomic ratio determined to be 1:2.7. For crystalline WS_2 QDs (purchased from Jiangsu XFNANO Materials Tech Co., Ltd., China), the relative content of W^{4+} increases to 51.8%, and the W/S atomic ratio is 1:2.1 (**Supplementary Figs. 3 and 4**), which is close to the stoichiometric ratio of 1:2. The comparison data are summarized in **Supplementary Table 1**.

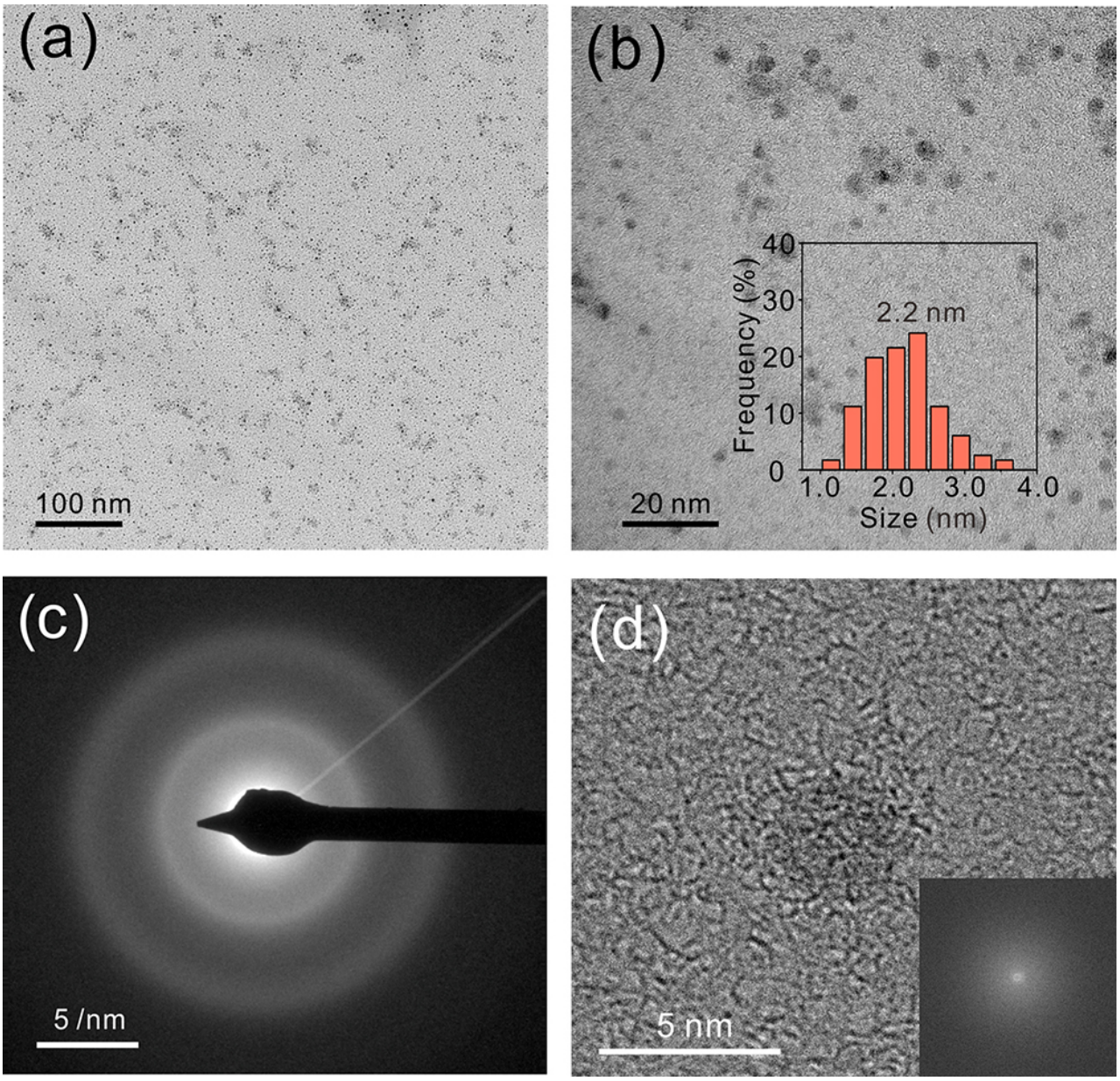


Fig. 3. TEM images, size distributions, and SAED pattern of amorphous WS_2 QDs. (a) Low-magnification TEM image, scale bar = 100 nm, (b) TEM image and size distribution, scale bar = 20 nm, (c) SAED pattern, scale bar = 5 nm^{-1}, (d) HRTEM image and fast Fourier transform (FFT) analysis of an individual amorphous WS_2 QD, scale bar = 5 nm. TEM, transmission electron microscopy.

TEM was used to investigate the morphologies of amorphous WS_2 QDs. As shown in Fig. 3a,b, the as-prepared WS_2 QDs are well dispersed with uniform sizes. A total of 50 individual QDs were counted to obtain the size distributions. The statistical size distributions show that the size of the WS_2 QDs is in the range of 1.2–3.6 nm, with an average of ~2.2 nm (Fig. 3b). TEM measurements of multiple batches of amorphous WS_2 QDs were carried out. Their size distributions fall within 1.8–4.2 nm (**Supplementary Fig. 5**), indicating favorable batch uniformity and stability. In the SAED pattern of WS_2 QDs (Fig. 3c), several diffuse diffraction rings are observed, indicating the amorphous phase of WS_2 QDs, which is consistent with the XRD results in Fig. 1a. In the HRTEM image of an individual amorphous WS_2 QD (Fig. 3d), no ordered and periodic lattice fringes are observed, indicating the absence of long-range crystalline order. Distinct diffraction spots are not observed in the corresponding fast Fourier transform (FFT) pattern, which further confirms the amorphous structure of WS_2 QDs. In contrast, the HRTEM image of crystalline WS_2 QDs exhibits clear lattice fringes (**Supplementary Fig. 6**).

In addition, AFM was used to characterize the morphology of amorphous WS_2 QDs. Fig. 4 shows the AFM image and the corresponding height profiles of the as-prepared WS_2 QDs. The height profiles show that the thick-

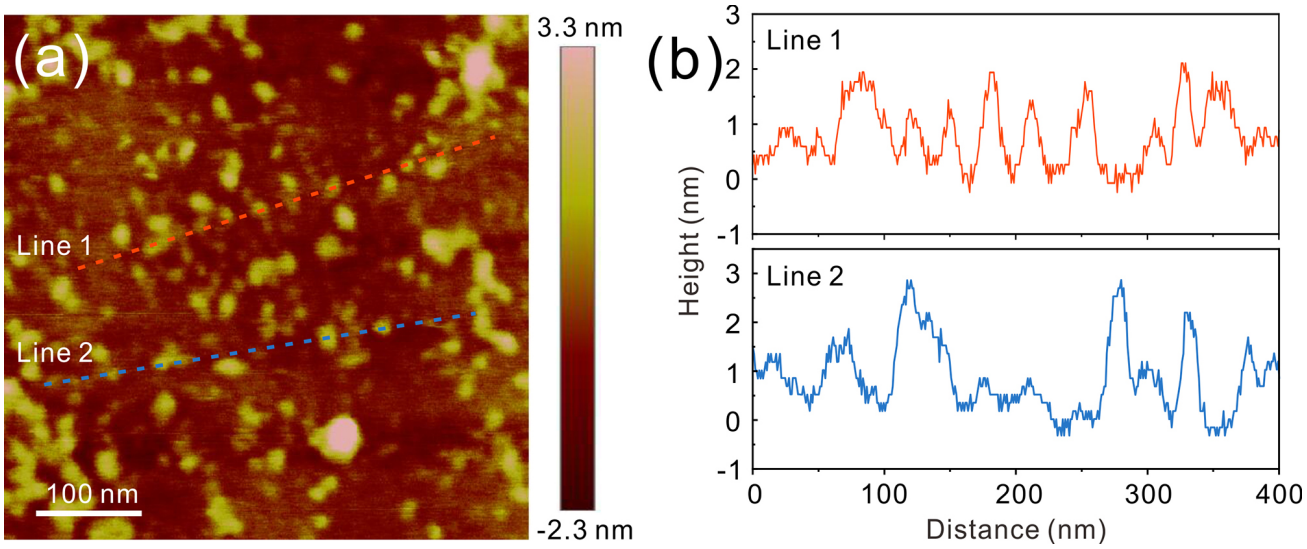


Fig. 4. AFM image of amorphous WS_2 QDs. (a) AFM image, (b) the height profiles performed along the lines in (a). AFM, atomic force microscopy.

ness of WS_2 QDs ranges from 1 to 3 nm, corresponding to 1–4 WS_2 layers, since the thickness of a monolayer of WS_2 is about 0.77 nm [34]. All the results indicate that the van der Waals forces between the layers of WS_2 are destroyed after ultrasonic treatment, verifying that amorphous WS_2 QDs are successfully synthesized.

To investigate the optical properties of amorphous WS_2 QDs, the UV-vis absorption spectrum was recorded in the range from 200 to 800 nm. Baseline correction was carried out prior to sample measurement. The pure solvent was scanned as a blank background, and its absorption signal was automatically subtracted to eliminate the absorption of the solvent. As shown in Fig. 5a, no obvious absorption peaks are observed in the visible range. Furthermore, the optical band gap (E_g) of amorphous WS_2 QDs was calculated using the Tauc plot [11,35]:

$$\alpha h\upsilon = (h\upsilon - E_g)^n \quad (1)$$

where α is the absorption coefficient, υ is the photon frequency, h is the Planck constant, and n can take the values 1/2, 3/2, 2, and 3 for direct allowed, direct forbidden, indirect allowed, and indirect forbidden transitions, respectively [36]. Bulk and few-layer TMDCs exhibit indirect band gaps, whereas monolayer TMDCs show direct band gaps. Therefore, the value of n is 2 for few-layered WS_2 QDs. The absorption coefficient α was converted from experimental absorbance based on the Beer-Lambert equation [37]:

$$\alpha = 2.303A/l \quad (2)$$

where l is the path length of the quartz cuvette (l = 1 cm) and A is the absorbance. Therefore, the average optical band gap of amorphous WS_2 QDs is 3.01 eV (Fig. 5b), which is much larger than that of bulk WS_2 (1.30 eV). We also compared the UV-vis absorption spectra and optical band gap results for amorphous and crystalline WS_2 QDs. Compared with amorphous WS_2 QDs, crystalline WS_2 QDs possess a smaller optical band gap (1.87 eV, **Supplementary Fig. 7**). This phenomenon mainly arises from the larger particle size of crystalline WS_2 QDs (~5 nm, **Supplementary Fig. 6**).

4. Discussion

4.1 Quantum Confinement Effect

The Bohr radius (R) can be expressed as [38]:

$$R = \varepsilon(\frac{m_0}{\mu})a_0 \quad (3)$$

where ε is the dielectric constant of the bulk material, m_0 is the free electron mass, a_0 = 0.053 nm, and μ is the reduced mass of the exciton (μ = 0.2 m_0 for WS_2). For bulk WS_2, the value of ε is 14 [38]. Therefore, the calculated Bohr radius R of WS_2 is ~3.7 nm. The quantum confinement effect can be expected as the average radius of the as-prepared WS_2 QDs (~1.1 nm) is below ~3.7 nm. In addition, the band gap (E*) for different particle sizes can be written as [12]:

$$E^* = E + \frac{h^2}{8\mu r^2} - \frac{1.8e^2}{4\pi r\varepsilon_0\varepsilon} \quad (4)$$

where E is the band gap of the bulk material, h is the Planck constant, r is the radius of the nanoparticle, μ is the reduced mass of the exciton, and ε_0 is the permittivity of free space.

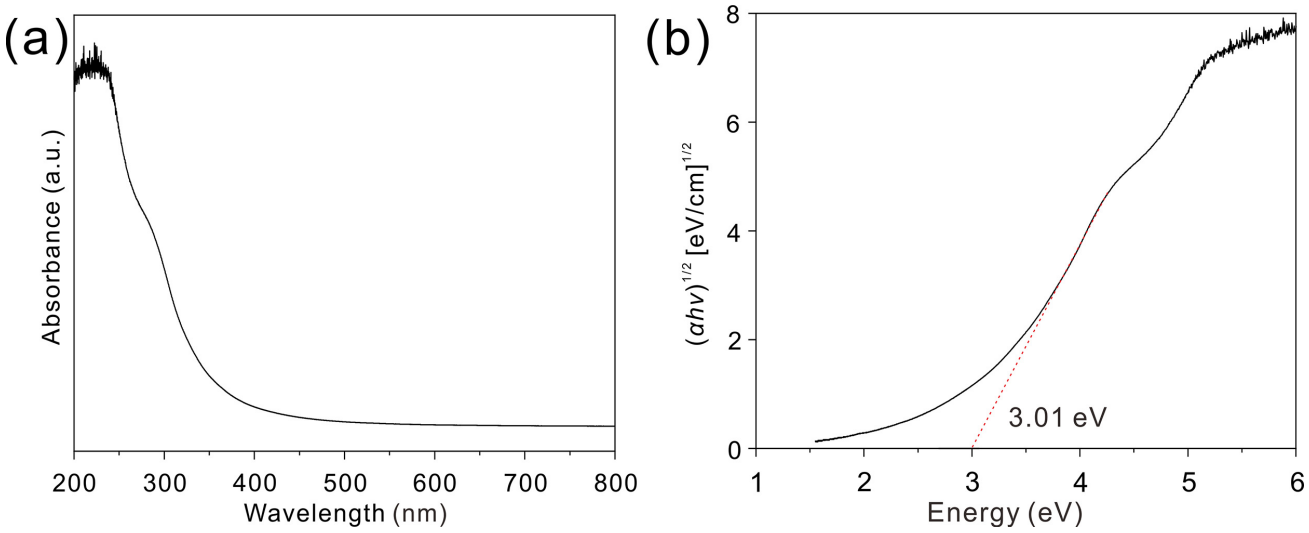


Fig. 5. Absorption spectrum of amorphous WS_2 QDs. (a) UV-vis absorption spectrum, (b) optical band gap energy of amorphous WS_2 QDs derived from (a).

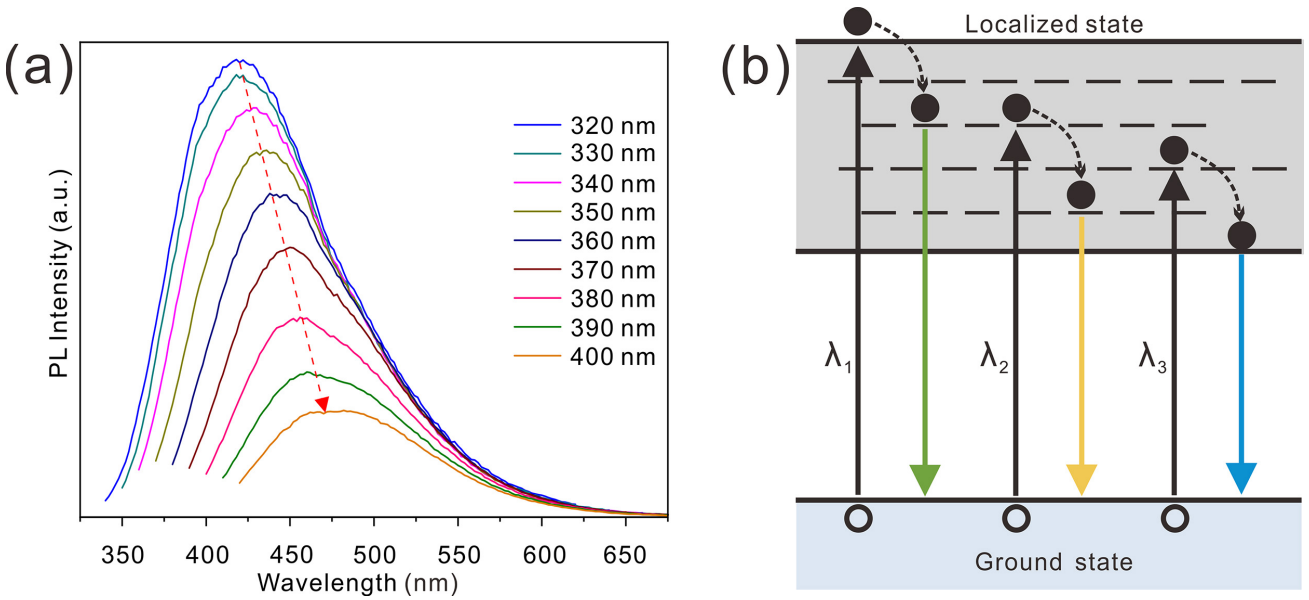


Fig. 6. The PL of amorphous WS_2 QDs. (a) The PL of amorphous WS_2 QDs at different excitation wavelengths, (b) schematic diagrams of the carrier recombination mechanism in amorphous WS_2 QDs. λ_1, λ_2, and λ_3 are defined as three distinct excitation wavelengths; the upward and downward arrows represent the excitation and emission processes, respectively.

Thus, materials with smaller dimensions exhibit a larger band gap. For bulk WS_2, the band gap is 1.30 eV. Based on the size distribution of the amorphous WS_2 QDs (Fig. 3b), the band gap distribution of amorphous WS_2 QDs ranges from 1.8–6.2 eV. The increase in optical band gap is not exclusively induced by quantum confinement. Other factors, such as amorphous structure, surface oxidation, structural defects, and surface states, may also shift the absorption edge and affect the band gap [39,40].

4.2 Excitation Wavelength-Dependent Photoluminescence Behavior

The PL spectra of amorphous WS_2 QDs were measured at excitation wavelengths ranging from 320 to 400 nm. As shown in Fig. 6a, the PL emission exhibits excitation-wavelength dependence, and the PL intensity decreases as the excitation wavelength increases. The maximum PL emission is located at 420 nm under 320 nm excitation. The photoluminescence excitation (PLE) spectrum of the amorphous WS_2 QDs (λ_{EM} = 420 nm) further confirms that excitation at ~320 nm produces the strongest emission at 420 nm (**Supplementary Fig. 8**). A possi-

ble mechanism is used to explain why the PL emission depends on the excitation wavelength in amorphous WS_2 QDs (Fig. 6b). Shorter excitation wavelengths correspond to higher excitation energy, which preferentially excites the smaller-sized WS_2 QDs with a larger band gap [12,41]. Conversely, longer excitation wavelengths can excite states with a smaller band gap in the nanomaterials. Under illumination, the carriers are generated and fall into the localized states. In localized states, the carriers either undergo radiative recombination or are scattered into other lower-energy localized states [19]. For localized states where carrier relaxation is slow and the relaxation time is constant, excited carriers at higher energy will recombine in higher localized states prior to relaxing to the lowest level, thereby emitting higher-energy photons. Correspondingly, the carriers with lower excitation energy relax to lower localized states, accompanied by the emission of low-energy photons. Thus, the energy of the emitted PL photons is correlated with the excitation energy, which gives rise to excitation-wavelength-dependent PL. The PL spectra of amorphous WS_2 QDs under different excitation wavelengths were re-measured after one month of storage, and similar data were obtained (**Supplementary Fig. 9**), demonstrating the stable PL performance of the as-prepared amorphous WS_2 QDs.

4.3 Limitations

Although the present research details the successful synthesis of amorphous WS_2 QDs via a facile ultrasonic liquid-phase exfoliation, several limitations should be noted. The effects of crystalline and amorphous phases on the intrinsic properties of WS_2 QDs are not sufficiently explored. The discussion on practical applications of the amorphous WS_2 QDs is insufficient.

5. Conclusions

In summary, a facile ultrasonic liquid-phase exfoliation method for the synthesis of amorphous WS_2 QDs has been reported. The structure, composition, size distribution, and absorption band edge of amorphous WS_2 QDs were characterized by XRD, XPS, Raman, TEM, and UV-vis spectroscopy. The amorphous WS_2 QDs show a narrow size distribution with an average diameter of 2.2 nm, and the thickness is 1–3 nm. Compared with bulk WS_2, these ultrasmall amorphous WS_2 QDs exhibit a wider optical band gap of 3.01 eV, mainly owing to the quantum confinement effect. The amorphous WS_2 QDs exhibit the maximum PL intensity under an excitation wavelength of 320 nm. Excitation wavelength-dependent PL is observed, which is tentatively attributed to the recombination of carriers from the localized states. This work provides a simple route to synthesize size-uniform amorphous WS_2 QDs with promising prospects in optoelectronic devices.

Availability of Data and Materials

The data supporting the findings and methodologies presented in this study are available from the corresponding authors upon reasonable request. Any additional materials referenced in this article are publicly accessible.

Author Contributions

LL: Conceptualization, Supervision, Methodology, Investigation, Visualization, Formal Analysis, Writing–Original Draft, Writing–Review & Editing, Project Administration. YM: Investigation, Data Curation, Formal Analysis, Visualization, Writing–Review & Editing. JG: Supervision, Software, Methodology, Formal Analysis, Resources, Writing–Review & Editing. BY: Supervision, Formal Analysis, Methodology, Project Administration, Resources, Funding Acquisition, Writing–Review & Editing. XF: Investigation, Methodology, Validation, Visualization, Data Curation, Writing–Review & Editing. GL: Conceptualization, Supervision, Visualization, Project Administration, Resources, Funding Acquisition, Writing–Review & Editing. All authors read and approved the final manuscript. All authors have participated sufficiently in the work and agreed to be accountable for all aspects of the work.

Ethics Approval and Consent to Participate

Not applicable.

Acknowledgment

We gratefully acknowledge the assistance and instruction from Ms. Mengyan Chen of the Shiyanjia Lab for XPS measurements. The graphical abstract was created by the authors using Origin and CorelDRAW.

Funding

This research was funded by the Scientific Research Foundation for High-level Talents of Anhui University of Science and Technology (Grant No. 2022yjrc91), the National Natural Science Foundation of China (Grant No. 12304437) and the Anhui Postdoctoral Scientific Research Program Foundation (Grant No. 2026C1481).

Conflicts of Interest

Leilei Lan and Baichun Yao have a financial relationship with the company. However, the company had no role in the handling or conduct of the study. The authors had full access to all data in the study and take full responsibility for the integrity of the data and the accuracy of the data analysis.

Supplementary Material

Supplementary material associated with this article can be found, in the online version, at https://doi.org/10.31083/DJNB56453.

References

[1] Zhu J, Li W, Zhang C, Li A, Luo R, Zhou S, et al. Mechanistic Insights into Dislocation-Mediated Single-Atom Doping of 2D Transition Metal Dichalcogenides. Advanced Functional Materials. 2026; 36: e21463. https://doi.org/10.1002/adfm.202521463

[2] Suonan Z, Wu H, Mi S, Xu H, Xu H, Zhang H, et al. Controllable growth of large 1T-NbTe2 nanosheets on mica by chemical vapor deposition and its magnetic properties. Journal of Crystal Growth. 2024; 648: 127891. https://doi.org/10.1016/j.jcrysgro.2024.127891

[3] Zhu Z, Chen L, Liu X, Wang H, Xu C, Yan Z, et al. Breaking the Trade-off: Bulk 2D Ising Superconductivity with High Tc and Giant Interlayer Spacing via a Unique Chain Intercalation in (BaS)1/3TaS2. Journal of the American Chemical Society. 2026; 148: 20622–20630. https://doi.org/10.1021/jacs.6c01737

[4] Son E, Lee S, Seo J, Kim U, Kim SH, Baik JM, et al. Engineering the Local Atomic Configuration in 2H TMDs for Efficient Electrocatalytic Hydrogen Evolution. ACS Nano. 2023; 17: 10817–10826. https://doi.org/10.1021/acsnano.3c02344

[5] Tang X, Hao Q, Hou X, Lan L, Li M, Yao L, et al. Exploring and Engineering 2D Transition Metal Dichalcogenides toward Ultimate SERS Performance. Advanced Materials (Deerfield Beach, Fla.). 2024; 36: e2312348. https://doi.org/10.1002/adma.202312348

[6] Lin H, Zhang Z, Zhang H, Lin KT, Wen X, Liang Y, et al. Engineering van der Waals Materials for Advanced Metaphotonics. Chemical Reviews. 2022; 122: 15204–15355. https://doi.org/10.1021/acs.chemrev.2c00048

[7] Tang X, Fan X, Zhou J, Wang S, Li M, Hou X, et al. Alloy Engineering Allows On-Demand Design of Ultrasensitive Monolayer Semiconductor SERS Substrates. Nano Letters. 2023; 23: 7037–7045. https://doi.org/10.1021/acs.nanolett.3c01810

[8] Li M, Gao Y, Fan X, Wei Y, Hao Q, Qiu T. Origin of layer-dependent SERS tunability in 2D transition metal dichalcogenides. Nanoscale Horizons. 2021; 6: 186–191. https://doi.org/10.1039/d0nh00625d

[9] Zou X, Zhao Y, Fan D, Wu S, Wang Y, Zou C, et al. Robust epitaxy of single-crystal transition-metal dichalcogenides on lanthanum-passivated sapphire. Science (New York, N.Y.). 2025; 390: eaea0849. https://doi.org/10.1126/science.aea0849

[10] Li Q, Wu K, Zhu H, Yang Y, He S, Lian T. Charge Transfer from Quantum-Confined 0D, 1D, and 2D Nanocrystals. Chemical Reviews. 2024; 124: 5695–5763. https://doi.org/10.1021/acs.chemrev.3c00742

[11] Soltabayev B, Tangirbergen A, Abdumutaliyeva D, Rakhmanova A, Kenzhebek M, Acar S, et al. Two-dimensional ZnO nanosheets synthesized by the SILAR method: Structural, optoelectronic, and gas-sensing properties. Colloids and Surfaces A: Physicochemical and Engineering Aspects. 2026; 743: 140528. https://doi.org/10.1016/j.colsurfa.2026.140528

[12] Gan ZX, Liu LZ, Wu HY, Hao YL, Shan Y., Wu XL, et al. Quantum confinement effects across two-dimensional planes in MoS2 quantum dots. Applied Physics Letters. 2015; 106: 233113. https://doi.org/10.1063/1.4922551

[13] Xu Y, Wang X, Zhang WL, Lv F, Guo S. Recent progress in two-dimensional inorganic quantum dots. Chemical Society Reviews. 2018; 47: 586–625. https://doi.org/10.1039/c7cs00500h

[14] Zhang MM, Peng F, Hu BZ, Lian Y, Wang HM, Wang HL. Dual-emission ratiometric fluorescence sensor based on CeO 2 quantum dots for the rapid detection of norfloxacin. Digest Journal of Nanomaterials & Biostructures (DJNB). 2025; 20: 753.

[15] Kundu B, Özdemir O, Dalmases M, Kumar G, Konstantatos G. Hybrid 2D-QD MoS 2 –PbSe Quantum Dot Broadband Photodetectors with High-Sensitivity and Room-Temperature Operation at 2.5 µm. Advanced Optical Materials. 2021; 9: 2101378. https://doi.org/10.1002/adom.202101378

[16] Tang X, Zeng X, Liu H, Yang Y, Zhou H, Cai H. A nanohybrid composed of MoS2 quantum dots and MnO2 nanosheets with dual-emission and peroxidase mimicking properties for use in ratiometric fluorometric detection and cellular imaging of glutathione. Mikrochimica Acta. 2019; 186: 572. https://doi.org/10.1007/s00604-019-3660-x

[17] Zhao M, Chen AY, Huang D, Chai YQ, Zhuo Y, Yuan R. MoS2 Quantum Dots as New Electrochemiluminescence Emitters for Ultrasensitive Bioanalysis of Lipopolysaccharide. Analytical Chemistry. 2017; 89: 8335–8342. https://doi.org/10.1021/acs.analchem.7b01558

[18] Lian H, Pan M, Han J, Cheng X, Liang J, Hua W, et al. A MoSe 2 quantum dot modified hole extraction layer enables binary organic solar cells with improved efficiency and stability. Journal of Materials Chemistry A. 2021; 9: 16500–16509. https://doi.org/10.1039/d1ta04030h

[19] Singh VK, Mishra H, Ali R, Umrao S, Srivastava R, Abraham S, et al. In Situ Functionalized Fluorescent WS2-QDs as Sensitive and Selective Probe for Fe3+ and a Detailed Study of Its Fluorescence Quenching. ACS Applied Nano Materials. 2019; 2: 566–576. https://doi.org/10.1021/acsanm.8b02162

[20] Lian S, Liu Z, Fu X, Zhu F, Zhang J, Cao G, et al. Nanoresonance Cavity and Localized Surface Plasmon Resonance Enhanced Broad-Spectral Photodetector for Versatile Applications. Nano Letters. 2025; 25: 6583–6591. https://doi.org/10.1021/acs.nanolett.5c00479

[21] Debnath S, Ghosh K, Meyyappan M, Giri PK. A fully printed ultrafast Si/WS2 quantum dot photodetector with very high responsivity over the UV to near-infrared region. Nanoscale. 2023; 15: 13809–13821. https://doi.org/10.1039/d3nr02331a

[22] Rai S, Singh VK, Chauhan BS, Srikrishna S., Saxena PS, Srivastava A. Functionalized WS2 Quantum Dots as Fluorescent Nanoprobes for In Vivo Bioimaging. ACS Applied Nano Materials. 2023; 6: 17657–17667. https://doi.org/10.1021/acsanm.3c02883

[23] Cheng ZL, Ma L, Liu Z. Hydrothermal-assisted grinding route for WS2 quantum dots (QDs) from nanosheets with preferable tribological performance. Chinese Chemical Letters. 2021; 32: 583–586. https://doi.org/10.1016/j.cclet.2020.02.002

[24] Caigas SP, Santiago SRM, Lin TN, Lin CAJ, Yuan CT, Shen JL, et al. Origins of excitation-wavelength-dependent photoluminescence in WS2 quantum dots. Applied Physics Letters. 2018; 112: 092106. https://doi.org/10.1063/1.5009638

[25] Caigas SP, Cheng MC, Lin TN, Santiago SRMS, Yuan CT, Yang CC, et al. P-Type Doping of WS2 Quantum Dots via Pulsed Laser Ablation. ACS Photonics. 2018; 5: 4828–4837. https://doi.org/10.1021/acsphotonics.8b00941

[26] Lee HJ, Choe M, Yang W, Lee SW, Park YJ, Hwang H, et al. Phase-Engineered WS2 Monolayer Quantum Dots by Rhenium Doping. ACS Nano. 2023; 17: 25731–25738. https://doi.org/10.1021/acsnano.3c11086

[27] Kang J, Li F, Xu Z, Chen X, Sun M, Li Y, et al. How Amorphous Nanomaterials Enhanced Electrocatalytic, SERS, and Mechanical Properties. JACS Au. 2023; 3: 2660–2676. https://doi.org/10.1021/jacsau.3c00418

[28] Li H, Zeng W, Zhao Z, Zheng M, Zhao J, Zhang W, et al. Intelligent Temperature Monitoring for Microfluidic System Using Mo 0.5 W 0.5 S 2 -Polymer Composite Based Memristive Sensory Neurons. Advanced Functional Materials. 2026; 36: e21525. https://doi.org/10.1002/adfm.202521525

[29] Michail A, Anestopoulos D, Delikoukos N, Grammatikopoulos S, Tsirkas SA, Lathiotakis NN, et al. Tuning the Photoluminescence and Raman Response of Single-Layer WS2 Crystals Using Biaxial Strain. The Journal of Physical Chemistry C. 2023; 127: 3506–3515. https://doi.org/10.1021/acs.jpcc.2c06933

[30] Miao W, Gai X, Zhao F, Wang J. Excitation induced asymmetric fluorescence emission in 2D-WS 2 quantum dots. Materials Advances. 2022; 3: 1772–1779. https://doi.org/10.1039/d1ma01178b

[31] Selvamani M, Krishnamoorthy G, Ramadoss M, Sivakumar PK, Settu M, Ranganathan S, et al. Ag@Ag8W4O16 nanoroasted rice beads with photocatalytic, antibacterial and anticancer activity. Materials Science & Engineering. C, Materials for Biological Applications. 2016; 60: 109–118. https://doi.org/10.1016/j.msec.2015.11.002

[32] Zeng T, Tang M, Luo L, Wu L, Chen M, Fu S, et al. 1T-WS2 Nanosheet-Modified Biomass Carbon as Sulfur Host for High-Performance Lithium–Sulfur Batteries. Advanced Engineering Materials. 2023; 25: 2300542. https://doi.org/10.1002/adem.202300542

[33] Park J, Cho I, Jeon H, Lee Y, Zhang J, Lee D, et al. Conversion of Layered WS2 Crystals into Mixed-Domain Electrochemical Catalysts by Plasma-Assisted Surface Reconstruction. Advanced Materials (Deerfield Beach, Fla.). 2024; 36: e2314031. https://doi.org/10.1002/adma.202314031

[34] Iqbal MW, Iqbal MZ, Khan MF, Shehzad MA, Seo Y, Park JH, et al. High-mobility and air-stable single-layer WS2 field-effect transistors sandwiched between chemical vapor deposition-grown hexagonal BN films. Scientific Reports. 2015; 5: 10699. https://doi.org/10.1038/srep10699

[35] Rong A, Zhao Q, Shi H, Cai X, Zhu H, Chen C, et al. Fabrication of CoTiO3/MgIn2S4 S–scheme heterojunctions with efficient charge separation to enhance the photocatalytic activities of hydrogen generation and formaldehyde removal. Separation and Purification Technology. 2025; 356: 130010. https://doi.org/10.1016/j.seppur.2024.130010

[36] Khan GA, Hogarth CA. Optical absorption spectra of evaporated V2O5 and co-evaporated V2O5/B2O3 thin films. Journal of Materials Science. 1991; 26: 412–416. https://doi.org/10.1007/bf00576535

[37] Abrinaei F, Kimiagar S, Zolghadr S. Hydrothermal synthesis of hematite-GO nanocomposites at different GO contents and potential application in nonlinear optics. Optical Materials. 2019; 96: 109285. https://doi.org/10.1016/j.optmat.2019.109285

[38] Sharma S, Singh J, Bhagat S, Singh M, Sharma S. Size-tunable photoluminescence from WS 2 nanostructures. Materials Research Express. 2018; 5: 045047. https://doi.org/10.1088/2053-1591/aabdcd

[39] Van Troeye B, Ducry F, Dossena M, Luisier M, Afzalian A, Pourtois G. Impact of Interface and Surface Oxide Defects on WS2 Electronic Properties from First Principles. ACS Nano. 2025; 19: 11664–11674. https://doi.org/10.1021/acsnano.4c08959

[40] Shi Z, Ge H, He Y. The emergence of amorphous materials approaching the single-layer limit. Chemical Science. 2025; 16: 16392–16413. https://doi.org/10.1039/d5sc02419f

[41] Liu Q, Hu C, Wang X. A facile one-step method to produce MoS 2 quantum dots as promising bio-imaging materials. RSC Advances. 2016; 6: 25605–25610. https://doi.org/10.1039/c6ra00572a